Background Pressure Effects on the Performance of a 20 kW Magnetically Shielded Hall Thruster Operating in Various Configurations

Antonio Piragino [1,2,*,†], Farbod Faraji [1,†], Maryam Reza [1,†], Eugenio Ferrato [1,†], Annalisa Piraino [2] and Tommaso Andreussi [1,†]

1   SITAEL S.p.A., Via Alessandro Gherardesca 5, 56121 Pisa, Italy; farbod.faraji@sitael.com (F.F.); maryam.reza@sitael.com (M.R.); eugenio.ferrato@sitael.com (E.F.); tommaso.andreussi@sitael.com (T.A.)
2   Dipartimento Ingegneria Civile ed Industriale DICI, University of Pisa, Largo Lucio Lazzarino, 56122 Pisa, Italy; a.piraino@studenti.unipi.it
*   Correspondence: antonio.piragino@sitael.com
†   These authors contributed equally to this work.

Abstract: The paper reports the characterization results of a 20 kW-class magnetically shielded Hall thruster in three different configurations and operating with a centrally mounted cathode. The characterization was carried out at two different pumping speeds in SITAEL's IV10 vacuum chamber, resulting in two different background pressure levels for each tested operating point. A linear behavior of discharge current and thrust values versus the anode mass flow rate was noticed for both pumping speeds levels and for all the three configurations. In addition, the thrust and discharge current values were always found to be lower at lower background pressure levels. From the performance levels, a preliminary estimate of the ingested mass flow rates was performed, and the values were then compared to a recently developed background flow model. The results suggested that, for this thruster and in the tested operating regimes, the change in performance due to background pressure could be ascribed not only to the ingestion of external mass flow coming from the chamber but also to other physical processes caused by the flux of residual background neutrals.

1. Introduction

Advancements in space technologies have opened new perspectives for exploration and resource utilization in outer space. Among these technologies, electric propulsion is expected to be widely used in the near future [1,2]. Indeed, the Hall thruster technology [3] is already in use for satellite maneuvers, station-keeping, and large constellations [4]. Additionally, the developments of spacecraft power generation and management systems in recent years have augmented the available on-board power, which can be used to supply high-power Hall thrusters [5]

Over the last four decades, several high-power Hall thruster prototypes with nominal discharge powers higher than 10 kW have been developed and tested [6–15]. However, the complete development of such devices relies on the possibility of their testing in adequate on-ground vacuum facilities with proper pumping speed and dimensions. Examples of state-of-the-art vacuum chambers suited for high-power Hall thruster testing are NASA's Vacuum Facility 5 (VF5) and VF6 at Glenn Research Center (GRC) with a 700 m^3/s pumping speed on xenon [16,17], the Large Vacuum Test Facility (LVTF) at the University of Michigan [18], and the SITAEL's IV10 vacuum facility, the largest chamber for electric propulsion testing in Europe with a 6-m diameter and nearly 10-m length envelope [19].

Though these state-of-the-art chambers allow for vacuum pressures as low as 10^{-4} Pa when operating a high-power Hall thruster, these vacuum levels are still several orders of

magnitude higher than that of outer space. This relatively high residual pressure affects the performance characterization results in several ways. In the past, the Randolph's criterion [20] considered 6×10^{-3} Pa as a maximum limit in the background pressure for Hall thruster testing. Beyond this value, the ingested mass flow rate coming from the chamber would be larger than the accuracy of the standard laboratory mass flow controllers. However, this consideration was derived from a simple modeling of the random thermal flux of the neutrals inside the chamber.

More recent studies have highlighted that, even when operating at pressure levels below Randolph's criterion, thruster performance is still affected by pressure [21,22]. The operation of the thruster can be affected by a linear increase of thrust and discharge current with pressure when operating at constant mass flow rates or a decrease of the needed anode mass flow rate to get the same current when characterizing at constant power [23–26]. This behavior has been explained by the ingestion of the residual neutrals in the facility artificially augmenting the thruster performance [20–27]. A direct assessment of the ingested neutral flow is difficult to perform, but an estimate can be done analyzing the performance change or having a better insight of the neutrals inside the chamber when the thruster is firing [28,29]. Recent studies have focused on various aspects such as the change of plasma proprieties in the acceleration region [30–32] or cathode coupling [33,34].

The recent developments of high-power Hall thrusters have posed new research questions. On the one hand, the increase of mass flow rates and thruster dimensions imposes the need for large vacuum facilities and high pumping speeds, which has a direct impact on the costs of thruster development and qualification. Besides the investment needed to setup a suitable test facility and the costs associated with its operation, state-of-the-art pumping technology imposes a lower boundary on the obtainable background pressure level. On the other hand, high-power thrusters target challenging performance metrics in terms of thrust efficiency and lifetime, so the impact of a high background pressure during the characterization and endurance testing may have a severe impact on thruster qualification. Regarding performance in space, an extrapolation of the performance to vacuum condition can be done, but it currently relies on performance fitting from data gathered over an ample range of pressure levels [35].

For a magnetically shielded 20 kW-class Hall thruster, the effects of the background pressure have never been assessed in detail, with the notable exception of the 12.5 kW HERMeS Hall thruster [36]. The characterization presented here for the 20 kW Hall thruster was tailored to study the effect over a broader range of anode mass flow rates (up to 35 mg/s) and featured three configurations with different channel frontal areas and lower pumping speeds of the vacuum chamber.

The aim of this work was to present the characterization results of a 20 kW magnetically shielded Hall thruster operating at two different chamber pumping speeds and to assess the possible mechanisms behind the observed change in performance due to the only change in background pressure. In order to do so, the characterization was conceived to be at constant anode and cathode mass flow rate levels, and the only parameter that changed for each operating point was the background pressure as a result of the 40% increase of the cryogenic pump surfaces.

In parallel, simple relations to model the thruster response in terms of thrust and discharge current were derived. Due to the relatively large frontal area of the thruster, the ingestion of the propellant could be important. The gathered performance data were later analyzed, and the ingested mass flow rate was assessed using a recently developed background flow model.

Accordingly, in this work, we summarize the results of the characterizations carried out on the second development model (DM) of the HT20k, the HT20kDM2. In Section 2, we present a brief description of the test setup and the theoretical models used in this work. In Section 3, we present the characterization campaign and the test results. Section 4 then discusses the test results, focusing on the chamber pressure and the effect of the two-

pumping surface configurations on thruster performance. Last, in Section 5 the conclusions are summarized.

2. Materials and Methods

2.1. HT20k Second Development Model, the HT20k DM2

The HT20k DM2 is the second development model in the SITAEL's 20 kW class Hall thruster family. The DM2 is a Hall thruster with a BN-SiO$_2$ ceramic channel and a magnetic circuit comprising electromagnets and ferromagnetic parts to generate the required magnetic field topology at the channel exit. Specifically, this thruster model features the magnetic shielding of the channel walls in order to significantly increase its lifetime in line with the stringent requirements of relevant application cases and mission scenarios [37]. The channel was redesigned to mimic the end-of-life condition by including a chamfer near the exit. The magnetic topology is shaped in a way that the magnetic line tangent to the walls' chamfer penetrates near the colder near-anode region. The magnetically shielded topology was derived from the studies on two different development models of the SITAEL's 5 kW-class Hall thruster, the HT5k. The HT5k demonstrated low electron temperatures, T_e, and plasma potentials nearly equal to the anode potential, along the channel chamfered region, which significantly reduced the channel erosion by ion bombardment [38–41].

The HT20k DM2 can be arranged in 3 different configurations, each one with different channel width b but equal mean channel diameter d. These configurations are named HT20k S (small), HT20k M (medium), and HT20k L (large) (see Figure 1) in the order of increasing b. In particular, the channel frontal area is $A_{exit} = \pi d b$, where $b_L = 1.135\, b_M$ and $b_S = 0.865\, b_M$.
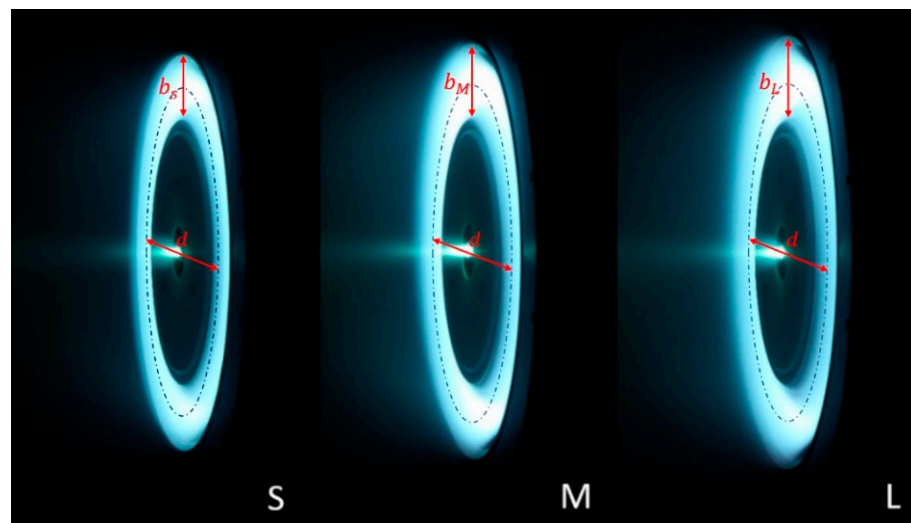

Figure 1. HT20k DM2 configurations: HT20k S (**left**), HT20k M (**middle**), and HT20k L (**right**) during firing.

In accordance with the difference in b, magnetic screens and poles are also modified to allow for the accommodation of the different channels and the implementation of the shielding field topology in all three configurations. The electromagnets and the back-plate of the magnetic circuit are the same as those in the unshielded HT20k version, the DM1, whose design and characterization results were reported in [42]. It must be said that the HT20k M retains the same channel dimensions of the HT20k DM1, and all three configurations have the same channel mean diameter d as the DM1.

The HT20k DM2 Hall thruster is coupled with the SITAEL HC60 high-current hollow cathode [43], which provides the electrons necessary to maintain the discharge and to neutralize the accelerated ion beam from the thruster.

2.2. Vacuum Facility, Electrical Configuration, and Diagnotics

The HT20k DM2 thruster unit was characterized in SITAEL's IV10 vacuum facility. During the firing of the thruster, the xenon propellant is pumped by condensation on cooled panels downstream the thruster exit at temperatures of about 30 K. Until 2018, the propellant coming from the thruster was pumped with 5 oxygen-free-copper cold panels (see [44] for further details). In February 2019, the number of cold panels was increased to 8, allowing for a higher flexibility in testing the thruster with different configurations of the pumping surfaces. Figure 2 shows the schematics of the vacuum chamber, and Table 1 presents its main operational characteristics.
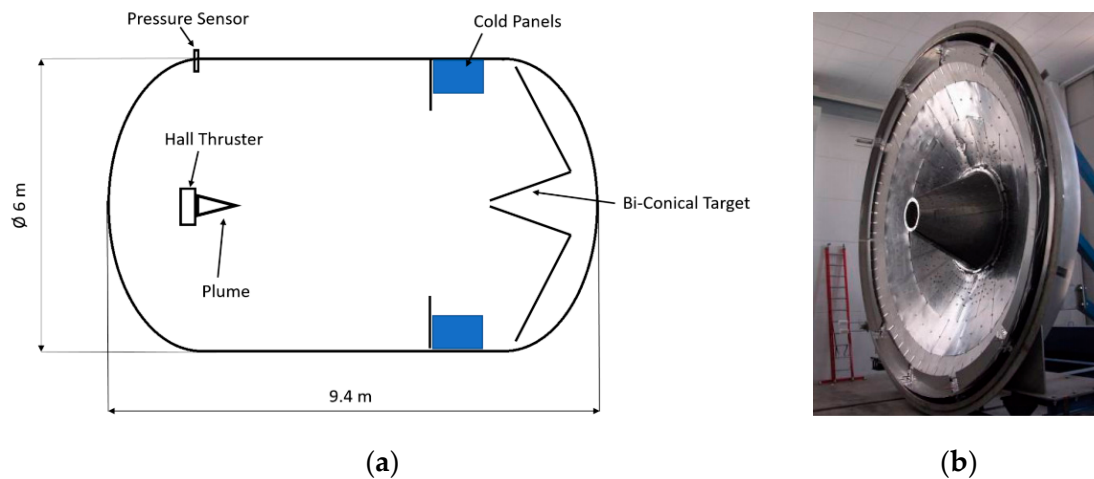

| (a) | (b) |

Figure 2. Schematic of the IV10 vacuum facility and its main dimensions (**a**). Opening cap and the bi-conical beam target (**b**).

Table 1. Main Characteristics of the IV10 vacuum chamber.

IV10 Vacuum Chamber Characteristics	
Inner diameter	5.47 m
Inner free diameter	5.4 m
Length of cylindrical section	6 m
Vacuum vessel total length	9.4 m
Free length for beam expansion	6.9 m
Internal free volume	160 m^3
Total leak rate	$<10^{-5}$ Pa·m^3·s^{-1}
Partial pressure (O$_2$, H$_2$O, N$_2$)	$<10^{-7}$ mbar
Pump down time	48 h

The entire internal surface of the chamber walls is cooled with liquid nitrogen (LN2) shrouds, keeping the wall temperatures at about 80 K with the firing thruster. In addition, an LN2-cooled bi-conical beam target (Figure 2) is housed on the opening cap of the facility. This bi-conical shape preferentially diverts the sputtered atoms towards the side walls instead of heading them back towards the thruster, and it increases the pumping capability of the cold panels (in Section 2.3, this is summarized as a sticking coefficient α). Moreover, all the critical surfaces undergoing significant bombardment from the thruster are lined up with Grafoil (purity > 99.9%) to reduce the back sputtering.

The pressure data presented in this work were taken using a Leybold ITR90 pressure sensor, located on the chamber wall at the position indicated in Figure 2. The pressure sensor is located nearly 3 m from the thruster, and it is positioned in a plane that comprises the thruster exit plane. The sensor is positioned towards the thruster. As stated by the manufacturer, the accuracy of the reading is ±15%.

The thruster discharge circuit was supplied using two Regatron TC.P.20.500.400.S laboratory-standard power supplies. Each power unit was a high-power DC supply

featuring a maximum voltage of 500 V and a maximum current of 50 A. Therefore, the two supplies were connected in parallel to provide the required discharge current compatible with high-power, low-voltage (<500 V) operating points.

As shown in Figure 3, no dedicated filter unit was implemented on the anode line for the test campaign described in this work. In the presented test, the filtering was performed by the internal capacitance of the two parallel supplies (84 μF each). The characterization of the HT20k DM2 with an RLC filter unit was carried out at one pumping speed, as described in [45], at discharge power levels up to 22.5 kW. Additionally, the thruster body was always grounded. Last, it must be said that the reading of the discharge current was ±0.5%.
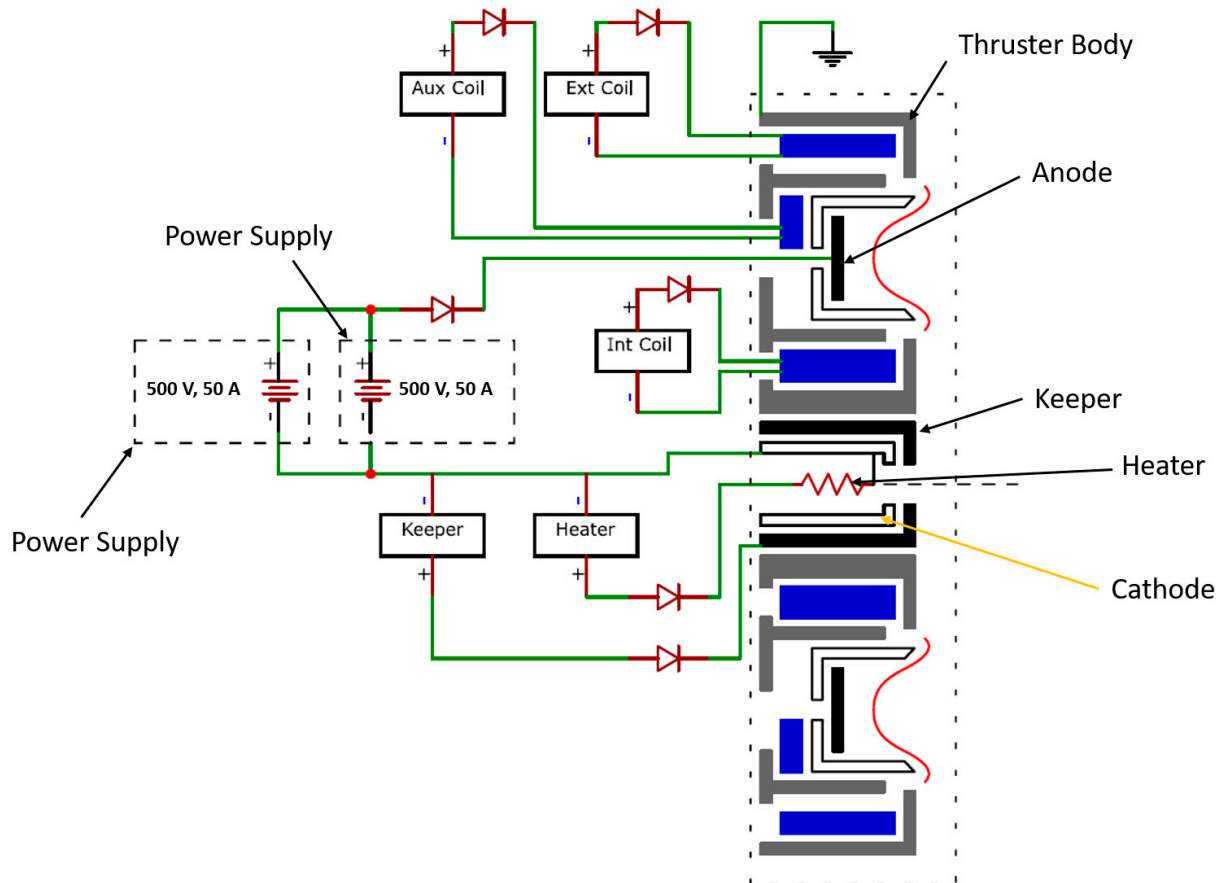

Figure 3. Electrical scheme—the thruster body was grounded.

Two separate laboratory mass flow controllers were used to provide the required xenon flow rate, the Bronkhorst F-201CV-500-AAD-88V for the anode and the Bronkhorst F-201C-FAC-88-V for the cathode, with an accuracy of 0.5% with respect to the set value.

The generated thrust was measured using a single axis thrust stand with a double pendulum configuration. The sensing element was based on high precision load cells measuring the strain on the flexural elements. The thrust stand was mounted on a tilting platform actuated by a stepper motor. This system allowed us to level the thrust stand during calibration. The thrust stand was also equipped with an electromagnetic calibrator, generating a reference force when requested. The calibrator was specifically built for the thrust stand; it is thermoregulated and has an accuracy in the order of 2‰ (2 parts per thousand). The calibration was performed at least twice a day, in cold and hot conditions for the thruster. The thrust measurement accuracy using this stand is ±10 mN. The thrust stand was also used during the test of the HT5k thruster, and there were no significant differences between the measured vales of thrust obtained in the same operating conditions with a different thrust stand [38,40,41].

The beam current density j was measured by a set of 18 Faraday probes, as shown in Figure 4. The probes were arranged on a circular rake, thus keeping the Faraday collectors surfaces at a distance R of 0.9 m from the center of the thruster. The probes were mounted at various azimuth angles φ ranging from $-90°$ to $+90°$. In addition, the rake also spanned in front of the thruster with an angle ϑ from $-90°$ to $+90°$.
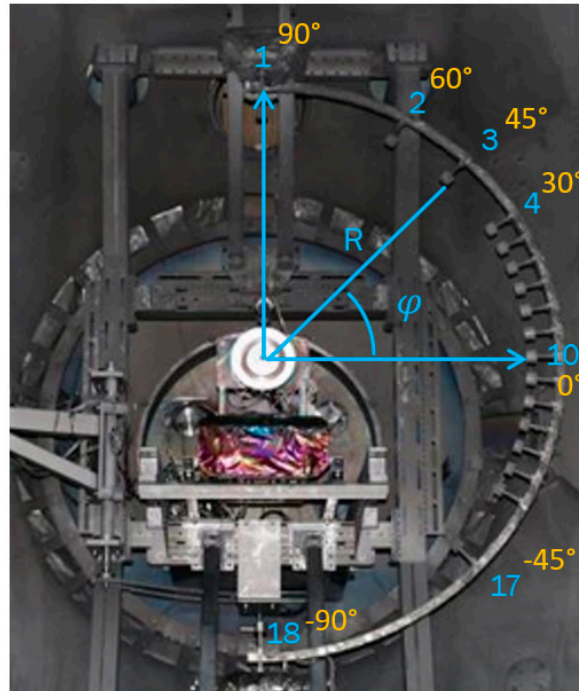

Figure 4. Faraday probes arrangement—the thruster is the HT5k [25].

The design of all the Faraday probes was the same of the one indicated as probe D in [46] (Centro Spazio/ALTA). In the calculation of the beam current I_{beam} and plume divergence λ, the geometric correction factors (here summarized with F) of [47] were used.

Considering the coordinate system introduced in Figure 4, the beam current I_{beam} was thus calculated according to the following integral:

$$I_{beam} = R^2 \int_{-\frac{\pi}{2}}^{\frac{\pi}{2}} \int_{-\frac{\pi}{2}}^{\frac{\pi}{2}} j(\vartheta, \varphi) F(\vartheta, \varphi) \cos\varphi \, d\vartheta \, d\varphi, \tag{1}$$

In addition, the divergence angle λ was calculated according to the procedure of [47].

The discharge current signal was captured using a multichannel Tektronix DPO 4104 oscilloscope with a current sensor on the anode line. The current probe has a DC limit of 100 A, with a typical error gain of less than 1%. The discharge current signal was sampled with a 1 MHz frequency.

2.3. Background Flow Model

The experimental campaign was carried out in SITAEL's IV10 vacuum facility, which can be run with different pumping surface arrangements. To investigate the influence of the pumping system on the thruster behavior, we used the 1D stationary background flow model developed by Frieman [48,49] as a generalization of a previous model developed by Cai [50]. In this work, we adapted the Frieman model to take the geometry of the IV10 vacuum chamber into account while only considering the downstream pumps.

In Figure 5, we introduce the surfaces C and D and the upstream and downstream directions, indicated, respectively, with (+) and (−). The surface D is the one that passes on the thruster exit plane. As indicated in [48], the plume is assumed to travel unimpeded through the opposite side of the chamber, where the ions neutralize and thermalize with

the velocity of the chamber walls. Some of the reflected particles condense on the pump surfaces, and the others go back and forth until they finally condense on the cold panels. As a result, in stationary conditions, there is a background flow from one end to the other of the chamber that may affect the thruster performance. The existence of this background flow is consistent with the simulation carried out by Cai [50].
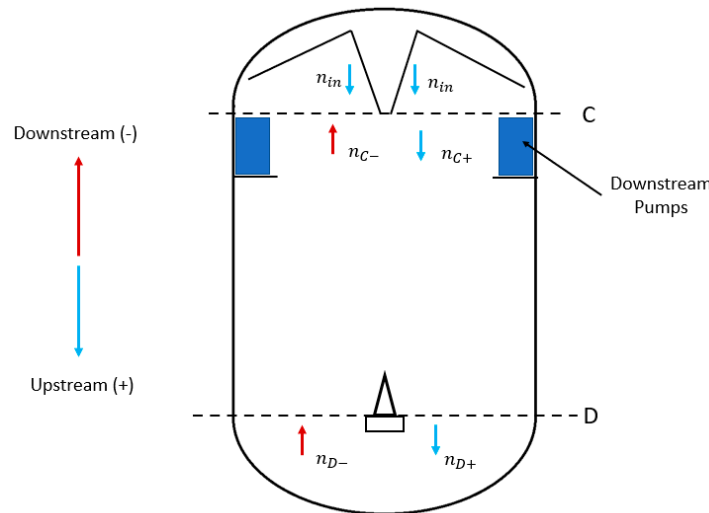

Figure 5. Schematics of the IV10 vacuum chamber and the parameters used for the 1D background flow model.

Recalling that the thruster exit plane is on the surface D, the total mass flow rate crossing the chamber on surface D in the (+) direction $F_D^{(+)}$ is:

$$F_{D+} = MS_c n_{c+} V_W - MS_{pd} n_{c+} V_W + (1-\alpha) n_{c+} S_{pd} M V_p \sqrt{\frac{T_w}{T_p}} \qquad (2)$$

In the above relation, M is the molecular mass of the background neutral, S_{pd} is the total area of downstream pump surfaces, α is the sticking coefficient of the pumps, and V_W and V_p are, respectively, the mean thermal diffusive velocities of particles in one direction when considering a Maxwellian particle distribution at chamber wall temperature T_W and pump temperature T_p [50]. V_W and V_p are defined as follows:

$$V_w = \sqrt{\frac{2kT_w}{\pi M}}, \ V_p = \sqrt{\frac{2kT_p}{\pi M}}, \qquad (3)$$

where k is the Boltzmann's constant.

In addition, since we only had downstream pumps, the parameter n_{c+}, relative to the number density of the particles crossing the surface C in the upstream direction, was modeled as follows:

$$n_C^{(+)} = \frac{n_{in}}{1 - (\alpha s_d - 1)^2}, \qquad (4)$$

where s_d is the ratio between the total surface area of downstream pumps S_{pd} and the chamber section S_C, and the input number density n_{in} is defined by the above assumption on plume reflection [49]; thus:

$$n_{in} = \frac{\dot{m}_{tot}}{MS_C} \sqrt{\frac{\pi M}{2kT_w}}. \qquad (5)$$

We consider all the mass flow rate injected into the chamber $\dot{m}_{tot} = \dot{m}_a + \dot{m}_{cathode}$, and, by substituting the $n_c^{(+)}$ and n_{in} in Equation (2), we get:

$$\frac{F_D^{(+)}}{\dot{m}_{tot}} = \frac{(1 - \alpha s_d)}{1 - (\alpha s_d - 1)^2}. \tag{6}$$

The ratio $\frac{F_D^{(+)}}{\dot{m}_{tot}}$ as a function of s_d and α is shown in Figure 6. As can be seen, the $F_D^{(+)}$ can be several times the actual mass flow rate injected into the chamber, depending on the sticking coefficient and surface ratio s_d of the pumps. Despite this, the ingested mass flow rate $\dot{m}_{ing}$ is a relatively small portion of the $F_D^{(+)}$, which depends on the thruster channel exit area A_{exit}. As suggested in [48,49], the ingested mass flow by the thruster can be computed by scaling the $F_D^{(+)}$ with the ratio A_{exit}/S_c.
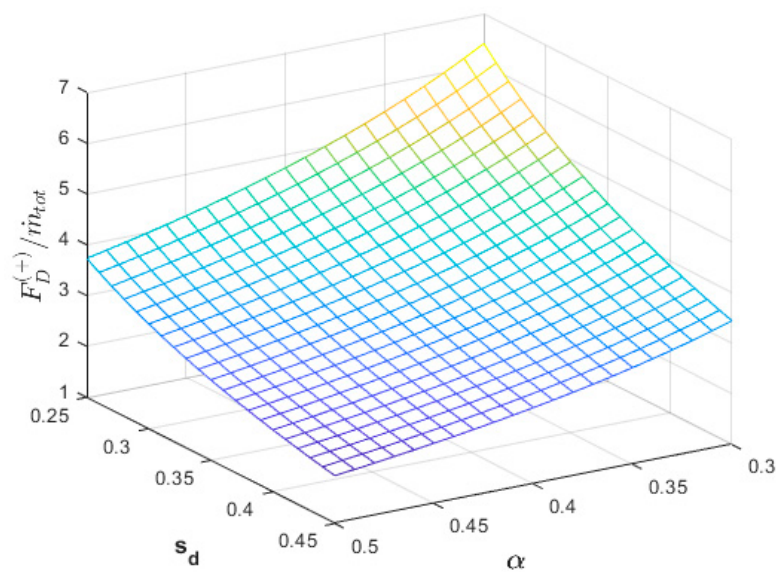

Figure 6. Ratio $F_D^{(+)}/\dot{m}_{tot}$ as a function of the sticking coefficient α and the surface ratio s_d for a vacuum chamber equipped only with downstream pumps.

We can thus say that a thruster with a fixed exit area A_{exit} at a fixed mass flow rate $\dot{m}_{tot}$ would experience a variation of ingested flow $\Delta \dot{m}_{ing}$ due to a change in the S_{pd}. In addition, the $\dot{m}_{ing}$ (and in the same way $\Delta \dot{m}_{ing}$) is proportional to the $\dot{m}_{tot}$ and the thruster exit area A_{exit}.

2.4. Thrust and Discharge Current

In this work, we modelled the thrust term using an approach similar to the one described in [51]. The thrust can be thought of as the sum of the contribution of each ion species i with the charge state Z_i and its relative ions mass flow rate $\dot{m}_{ji}$ accelerated through a potential drop $\eta_{vi} V_d$, where η_{vi} represents the so-called voltage utilization efficiency and V_d is the discharge voltage. Hence, we obtain:

$$T = \sum \left(\dot{m}_{ji} \sqrt{\frac{2e Z_i \eta_{vi} V_d}{M}} \right). \tag{7}$$

Assuming η_{vi} to be constant for all the ion species and to be equal to η_v, while also adding the beam divergence losses factor ψ_T, we multiply and divide each term of the summation by the total mass flow rate of the ions $\dot{m}_j$ to get:

$$T = \dot{m}_j \psi_T \sqrt{\frac{2e\eta_v V_d}{M}} \sum \left(\frac{\dot{m}_{ji}}{\dot{m}_j} \sqrt{Z_i} \right).$$

We now introduce $\xi_i = \frac{\dot{m}_{ji}}{\dot{m}_j}$ as the ratio between the mass flow rate of each ion species with the charge state Z_i and the total ion mass flow rate, and $\eta_m = \frac{\dot{m}_j}{\dot{m}}$ (ionization efficiency) is the ratio of the ionized mass flow rate to the mass flow rate processed by the thruster $\dot{m}$. The latter is the sum of the anode mass flow rate $\dot{m}_a$ and the ingested mass flow rate $\dot{m}_{ing}$, thus $\dot{m} = \dot{m}_a + \dot{m}_{ing}$. As a result, the thrust can then be written as:

$$T = \eta_m \psi_T \dot{m} \sqrt{\frac{2e\eta_v V_d}{M}} \sum \left(\xi_i \sqrt{Z_i} \right). \tag{8}$$

As for the beam current I_{beam}, which is the one contributing to the thrust, we can model it as the sum of the contribution of the beam current of each ion species with charge state Z_i and its relative mass flow rate $\dot{m}_{ji}$:

$$I_{beam} = \sum \left(\frac{\dot{m}_{ji}}{M} e Z_i \right). \tag{9}$$

We multiply and divide each term of the summation for $\dot{m}_j$ to obtain:

$$I_{beam} = \frac{\dot{m}_j e}{M} \sum \left(\frac{\dot{m}_{ji}}{\dot{m}_j} Z_i \right).$$

Recalling that the discharge current I_d can be thought as the sum contribution of the beam current I_{beam} plus the excess electron current I_e coming from the cathode (the latter sustaining the discharge), we get:

$$I_d = I_{beam} + I_e. \tag{10}$$

We now define the parameter $\eta_{current} = \frac{I_{beam}}{I_d}$ (current utilization efficiency), and recalling ξ_i and η_m, we obtain:

$$I_d = \frac{1}{\eta_{current}} \eta_m \dot{m} \frac{e}{M} \sum (\xi_i Z_i). \tag{11}$$

For sake of simplicity, we define the parameters:

$$\gamma_I = \frac{1}{\eta_{current}} \eta_m \frac{e}{M} \sum (\xi_i Z_i) \tag{12}$$

and

$$\gamma_T = \eta_m \psi_T \sqrt{\frac{2e\eta_v}{M}} \sum \left(\xi_i \sqrt{Z_i} \right) \tag{13}$$

to obtain simply:

$$I_d = \gamma_I \dot{m} \tag{14}$$

and

$$T = \gamma_T \dot{m} \sqrt{V_d}. \tag{15}$$

The above two relations are functions of the discharge voltage, the anode mass flow rate, the magnetic field peak intensity B at which the thruster operates, and the background pressure p.

3. Results

The HT20k DM2 was characterized at fixed values of anode mass flow rates $\dot{m}_a$ for all the three configurations (e.g., S, M, and L), as summarized in Table 2. The cathode mass flow rate $\dot{m}_{cat}$ was always kept at 8% of the $\dot{m}_a$, so $\dot{m}_{tot} = \dot{m}_a(1 + 0.08)$.

Table 2. Characterization matrix.

$\dot{m}_a$	250 V	300 V	400 V	500 V
20 mg/s		X		
25 mg/s	X	X	X	X
30 mg/s	X	X	X	X
35 mg/s	X	X	X	X

In the frame facility upgrade in February 2019 [52,53], we first characterized the points of Table 2 in IV10 pumping with five cold panels and then with IV10 pumping with seven cold panels. We noticed a reduction of the measured pressure at the same total mass flow rate $\dot{m}_{tot}$ (as depicted in Figure 7). During the characterization with five panels, the maximum background pressure was in the order of 2.8×10^{-3} Pa at $\dot{m}_{tot} = 37.8$ mg/s. The lowest recorded pressure levels were in the order of 9×10^{-4} Pa at $\dot{m}_{tot} = 21.6$ mg/s with seven panels.
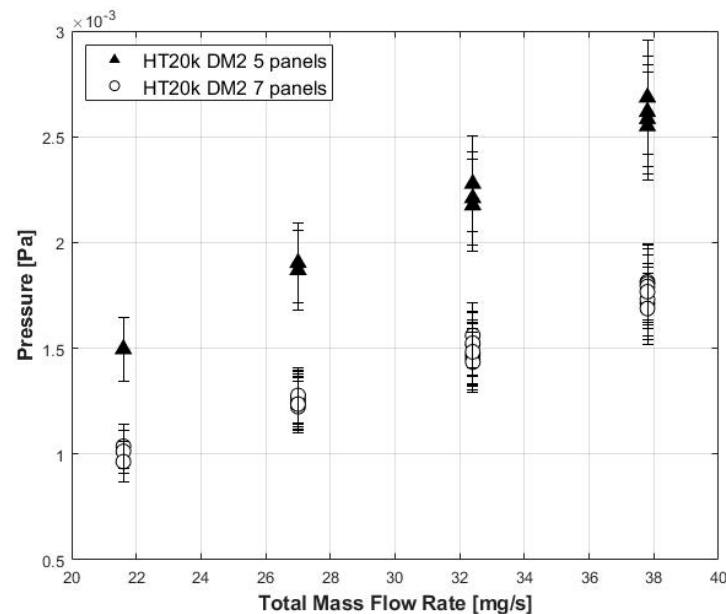

Figure 7. Comparison with the measured pressure with 5 and 7 cold panels as a function of the total mass flow rate.

The background pressure p versus total mass flow rate could be approximated as a linear trend, with different slopes when using five or seven cold panels. We can thus have an estimate of the sticking coefficient α by using the relation described in [50,54]:

$$\alpha = \dot{m}_{tot} \frac{\sqrt{2\pi R T_W}}{p S_{pd}}, \tag{16}$$

where the R is the gas constant for the specific gas (e.g., Xe) and T_W is the chamber walls temperature. The measurements taken with five panels and seven panels led to an average $\alpha = 0.420$.

The effective pumping speed of the chamber Q was calculated considering the method described in [55]:

$$Q = \frac{\dot{m}_{tot}}{p - p_{base}}. \tag{17}$$

The p_{base} is the pressure when the thruster is not operating and no mass flow rate is injected into the chamber, and it was found to equal 3×10^{-5} Pa, approximately two order of magnitude less than the measured pressures p. Consequently, the difference between the $p - p_{base}$ was nearly equal to p and well within the error of the measurement of the pressure sensor.

The pumping speed Q was calculated for all the operating points. The results led to an average Q value of 250 m^3/s with five panels and of 370 m^3/s with seven panels.

Thruster Performance

The operation of IV10 with seven cold panels resulted in a consistent loss of discharge current and thrust for all the operative conditions; as such, $I_d^{(5)} > I_d^{(7)}$ and $T^{(5)} > T^{(7)}$, where we introduced the notation $x^{(n)}$ to indicate that a parameter x is evaluated during operation with n cold panels.

The thrust and the discharge current were found to have a linear trend with respect to the anode mass flow rate or equivalently total mass flow rate, both for five and seven cold panel set-ups. For the sake of simplicity, we only show the results for the M configuration in Figure 8.
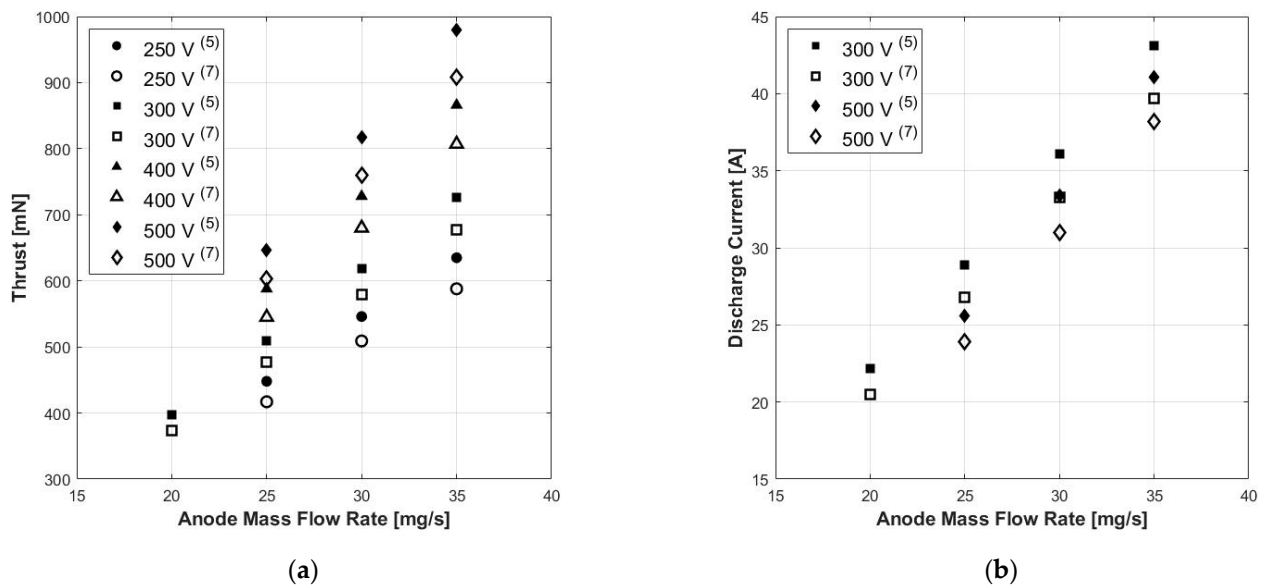

(a)   (b)

Figure 8. Measured thrust and discharge current for the HT20k M with 5 and 7 cold panels. The thrust levels are shown in (**a**) and the discharge current at 300 and 500 V in (**b**). Bold markers are relative to 5 panel operations, and the total mass flow rate was $\dot{m}_{tot} = \dot{m}_a(1 + 0.08)$. As can be seen, when the chamber was operating with 5 panels, the measured thrust and the discharge current were always larger.

Introducing the normalized delta quantities, defined for each operating point as follows,

$$\frac{\Delta I}{I} = \frac{I_d^{(5)} - I_d^{(7)}}{I_d^{(7)}}; \quad \frac{\Delta T}{T} = \frac{T^{(5)} - T^{(7)}}{T^{(7)}}, \tag{18}$$

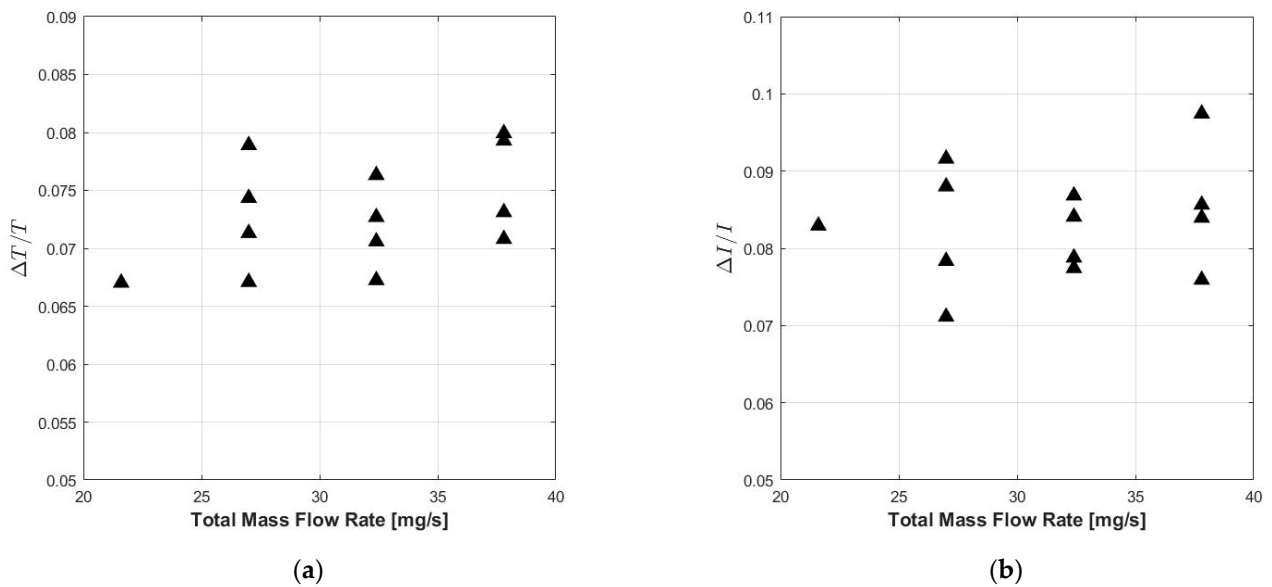we sum up the results for the M configurations in Figure 9.

(**a**)

(**b**)

Figure 9. Variations of thrust (**a**) and discharge current (**b**) as a function of the total mass flow rate for all the tested points on the HT20k M configuration. The changes stayed in the 6–8% range for the thrust and 7–10% for the discharge current.

We observed that the $\frac{\Delta T}{T}$ remained nearly constant with the total mass flow rate within the accuracy of the thrust balance. The same behavior for the $\frac{\Delta T}{T}$ was noticed for the HT20k S and HT20k L. The $\frac{\Delta I}{I}$ showed more dispersion as a function of the total anode mass flow, but it stayed within the error of the discharge current reading for each tested discharge voltage level ($\pm 0.5\%$).

The variation of the thrust (for the HT20k M) was in the order of 6–8%, and the variation of the discharge current was in the order of 7–10%, depending on the discharge voltage. Similar values were recorded for the other two configurations, as can be seen in Figure 10.
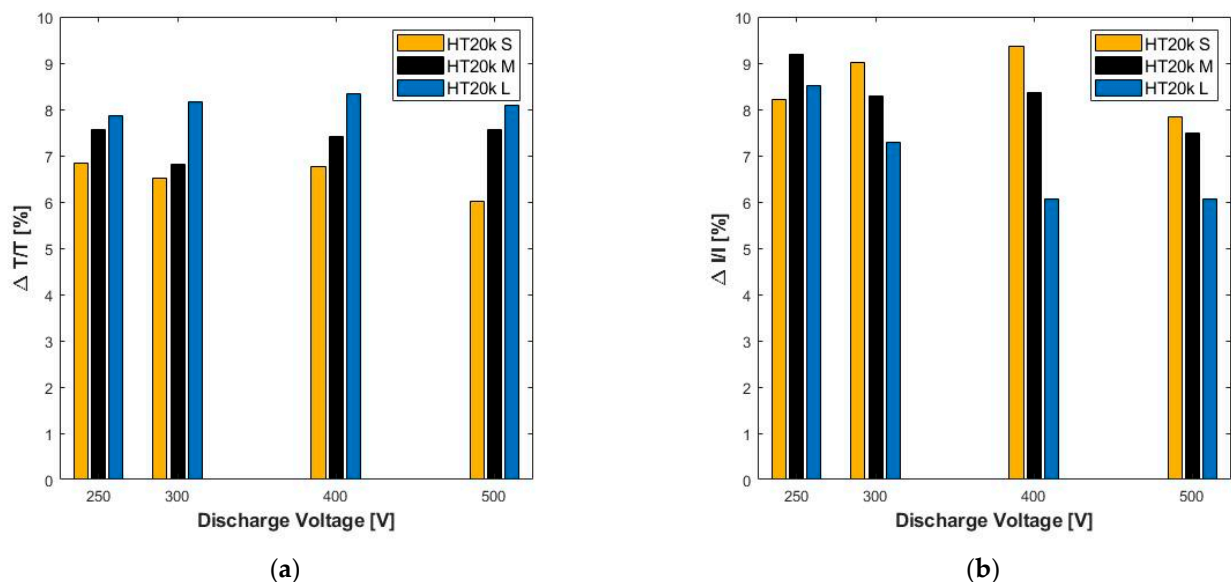

(**a**)

(**b**)

Figure 10. Average variations of thrust (**a**) and discharge current (**b**) for all the tested mass flow rates as a function of all the discharge voltage for all the tested points on the three thruster configurations. To sum up, the average changes stayed in the 6–8% range for the thrust and 6–9% for the discharge current.

The results of the Faraday probes are summarized in the Appendix A in terms of λ and $\eta_{current}$. The $\eta_{current}$ was found to be independent on the pump configuration.

For the plume divergence λ, even if the effect of the higher background pressure was noticed by a local increase of the current density due to the charge exchange (CEX) collisions at the wings of the plume [47], the measured divergence angle λ did not significantly change between the seven and five panel operations.

Regarding the discharge current, operations at higher pressure levels resulted in an increase of root mean square (RMS)signals for all the tested operating conditions. The results are summarized in the Appendix A.

The values of cathode to ground voltage (or cathode reference potential (CRP)) are summarized in the Appendix A. The difference of the CRP between the five and seven panel configurations was in the order of 2 V at most.

4. Discussion

For a Hall thruster, a generic response to an input (defined in terms of a change of anode mass flow rate, discharge voltage, magnetic field, or change in the background pressure) is a change in the thruster output performance, i.e., discharge current dI_d and thrust dT. The functional relations between inputs and outputs are generally non-linear and depend on the physical processes that occur in the thruster discharge. By considering a variation of an input, however, it is possible to evaluate the response of the system output through a linearization of these functional relations. Therefore, we can construct a series of differential relations that model the thruster response by using an approach similar to the one used so far in other type of electric propulsion devices [56].

In the case of the characterization presented in this work, we did not change the anode mass flow rate $d\dot{m}_a$, discharge voltage dV_d, and magnetic field peak dB for each operative point. Since we only changed the pumping surfaces (increasing them by 40%), we could write a system as a function only of the change in the background pressure dp, thus obtaining:

$$
\begin{cases}
dI_d = \left(\frac{\partial I_d}{\partial p}\right) dp \\
dT = \left(\frac{\partial T}{\partial p}\right) dp
\end{cases}.
\tag{19}
$$

Considering the discharge current and thrust modeled according to Equations (14) and 15, for a characterization at constant mass flow rates levels, we get:

$$
\begin{cases}
dI_d = \dot{m}\left(\frac{\partial \gamma_I}{\partial p}\right) dp + \gamma_I\left(\frac{\partial \dot{m}}{\partial p}\right) dp \\
dT = \dot{m}\sqrt{V_d}\left(\frac{\partial \gamma_T}{\partial p}\right) dp + \gamma_T\sqrt{V_d}\left(\frac{\partial \dot{m}}{\partial p}\right) dp
\end{cases},
\tag{20}
$$

where the terms $\frac{\partial \gamma_I}{\partial p}$ and $\frac{\partial \gamma_T}{\partial p}$ are, respectively, the variations of the γ_I and γ_T imposed by the change of pressure. The latter is not to be confused with the change of γ_I and γ_T due to the change in anode mass flow rate $\frac{\partial \gamma_I}{\partial \dot{m}_a}$ and $\frac{\partial \gamma_T}{\partial \dot{m}_a}$.

In addition, it has to be highlighted that the $\frac{\partial \gamma_I}{\partial p}$ and $\frac{\partial \gamma_T}{\partial p}$ may be different if the background pressure is modulated with different strategies, such as changing the number of pumping surfaces (the case of this work) or by artificially increasing the pressure by injecting xenon in one or multiple selected locations inside the chamber. In principle, the derivatives $\frac{\partial \gamma_I}{\partial p}$ and $\frac{\partial \gamma_T}{\partial p}$ can be also negative. Thus, we could have a loss of discharge current and/or thrust while increasing the pressure. This feature was not observed in this test campaign.

Additionally, the term $\frac{\partial \dot{m}}{\partial p}$ is indeed the actual change in the ingested mass flow rate due to the change in background pressure. Even in this case, the $\frac{\partial \dot{m}}{\partial p}$ can change if the background pressure is modulated with different strategies, as described before. The $\frac{\partial \dot{m}}{\partial p}$ is expected to be always positive.

By integrating from lower to higher pressure (from seven to five panel conditions) and assuming linear changes between the two pumping configurations of the chamber, we get:

$$
\begin{cases}
I_d^{(5)} - I_d^{(7)} = \left(\dot{m}_a + \dot{m}_{ing}^{(7)}\right)\left(\gamma_I^{(5)} - \gamma_I^{(7)}\right) + \gamma_I^{(7)}\Delta\dot{m}_{7-5} \\
T^{(5)} - T^{(7)} = \left(\dot{m}_a + \dot{m}_{ing}^{(7)}\right)\sqrt{V_d}\left(\gamma_T^{(5)} - \gamma_T^{(7)}\right) + \gamma_T^{(7)}\sqrt{V_d}\Delta\dot{m}_{7-5}
\end{cases}
\tag{21}
$$

By dividing the first part of Equation (21) by $I_d^{(7)} = \gamma_I^{(7)}\left(\dot{m}_a + \dot{m}_{ing}^{(7)}\right)$ and the second part by $T^{(7)} = \left(\dot{m}_a + \dot{m}_{ing}^{(7)}\right)\gamma_T^{(7)}\sqrt{V_d}$, we obtain the following system:

$$
\begin{cases}
\frac{I_d^{(5)} - I_d^{(7)}}{I_d^{(7)}} = \frac{\gamma_I^{(5)} - \gamma_I^{(7)}}{\gamma_I^{(7)}} + \frac{\Delta\dot{m}_{7-5}}{\left(\dot{m}_a + \dot{m}_{ing}^{(7)}\right)} \\
\frac{T^{(5)} - T^{(7)}}{T^{(7)}} = \frac{\gamma_T^{(5)} - \gamma_T^{(7)}}{\gamma_T^{(7)}} + \frac{\Delta\dot{m}_{7-5}}{\left(\dot{m}_a + \dot{m}_{ing}^{(7)}\right)}
\end{cases}
.
\tag{22}
$$

In principle, if the γ_I and γ_T are known, the $\dot{m}_{7-5}$ and $\dot{m}_{ing}^{(7)}$ can be calculated by solving the system of equations above. However, it is difficult to assess the exact values of γ_I and γ_T, even with a complete set of plasma and thruster diagnostics.

A preliminary estimate of the $\Delta\dot{m}_{7-5}$ can be done by focusing on the discharge current or thrust, assuming constant γ_I or γ_T and, in first approximation, neglecting $\dot{m}_{ing}^{(7)}$ in comparison to $\dot{m}_a$.

However, the $\Delta\dot{m}_{7-5}$ calculated with the assumptions of contant γ_I or γ_T with pressure and neglecting $\dot{m}_{ing}^{(7)}$ is not representative of the actual variation of the ingested mass flow rate; rather, it is an operative parameter used to justify the change in performace.

In this work, the $\Delta\dot{m}_{7-5}$ calculated with the assumption descrived above is called the apparent delta ingested mass flow rate, and it is indicated as $\Delta\dot{m}^{(app)}_{7-5}$. The $\Delta\dot{m}^{(app)}_{7-5}$ can be calculated from variations of the discharge current or from the variations of the thrust, and it leads to two differents $\Delta\dot{m}^{(app)}_{7-5}$ values for the same operative point. In particular, the $\Delta\dot{m}^{(app)}_{7-5}$ calculated from the $\frac{\Delta I}{I}$ showed a linear trend with the mass flow rate with a different gradient for each discharge voltage level, as can be seen from the nearly constant values of $\frac{\Delta I}{I}$ for each voltage level in Figure 12a. Additionally, since the recorded data of pressure are not dependant on the voltage (as also evidenced by the background flow model), the $\Delta\dot{m}^{(app)}_{7-5}$ should be only proportional to the total mass flow rate.

On the other hand, the $\Delta\dot{m}^{(app)}_{7-5}$ calculated from the $\frac{\Delta T}{T}$ only showed a clear linear trend with the $\dot{m}_{tot}$. For simplicity, the estimation of the $\Delta\dot{m}^{(app)}_{7-5}$ was thus performed and presented from the thrust varations using the following relation:

$$
\Delta\dot{m}^{(app)}_{7-5} = \frac{T^{(5)} - T^{(7)}}{T^{(7)}}\dot{m}_a.
\tag{23}
$$

The results of the $\Delta\dot{m}^{(app)}_{7-5}$ (calculated from the $\frac{\Delta T}{T}$ data) are shown in Figures 11 and 13 for all the three configurations of the HT20k DM2. In the figures, we also report the results of the background flow model multiplied by an amplification factor β that took an effective ingestion area βA_{exit} into account in orders to explain the computed values of $\Delta\dot{m}^{(app)}_{7-5}$. The A_{exit} is the actual annular surface at the channel exit. The modeled variation of ingested mass flow rate was calculated as follows:

$$
\overline{\Delta\dot{m}} = \left(\frac{F_{D+}^{(5)}}{S_c} - \frac{F_{D+}^{(7)}}{S_c}\right)\beta A_{exit},
\tag{24}
$$

where we used the parameters summarized in Table 3 to model the IV10 vacuum chamber. The parameter β was kept same for all thruster configurations and was calibrated in order to minimize the standard deviation for the difference between $\Delta\dot{m}^{(app)}_{7-5}$ and $\overline{\Delta\dot{m}}$ for all the tested points. For each configuration, we used the corresponding A_{exit}.
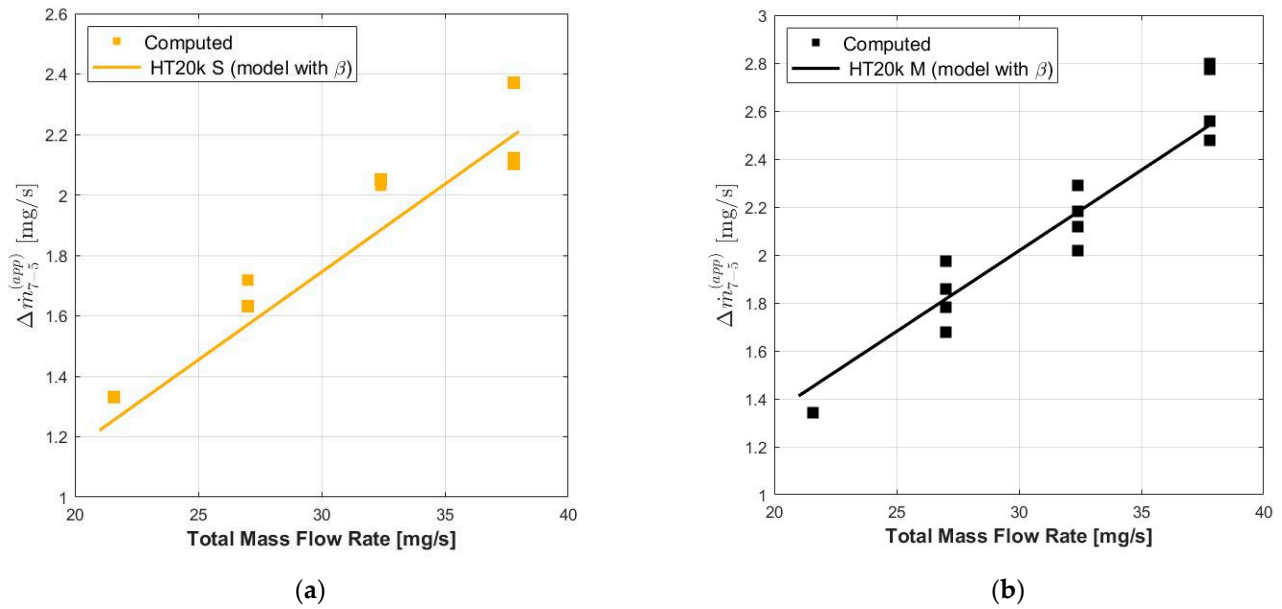

(a)

(b)

Figure 11. Apparent variation of ingested mass flow rate, indicated as $\Delta\dot{m}^{(app)}_{7-5}$ calculted for the thrust variations and comparison with the background flow model (with an amplitication factor $\beta = 49.6$) for HT20k S (**a**) and HT20k M (**b**).
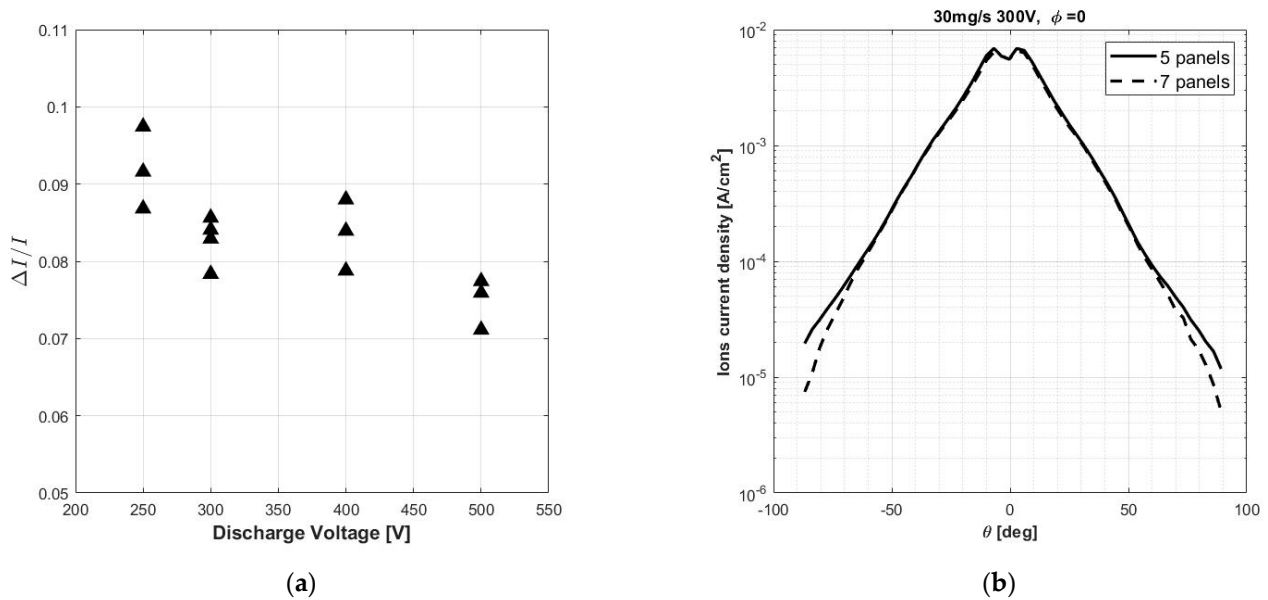

(a)

(b)

Figure 12. Variations of the discharge current as a function of the discharge voltage for the HT20k M configuration (**a**). Beam current density distribution for the for the Faraday probe at $\varphi = 0°$ for $\dot{m}_a = 30$ mg/s and $V_d = 300$ V with 5 and 7 cold panels (**b**).
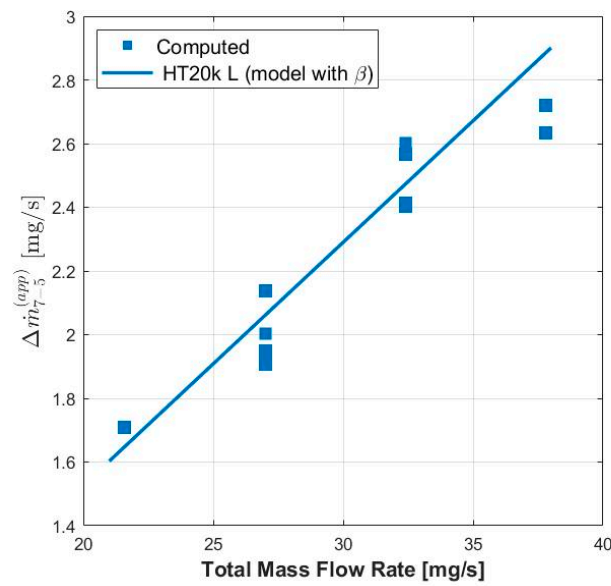
Figure 13. Apparent variation of ingested mass flow rate, indicated as $\Delta\dot{m}^{(app)}_{7-5}$ calculated from the thrust variations and comparison with the background flow model (with an amplitication factor $\beta = 49.6$) for HT20k L.

Table 3. Background flow model and summary of the used parameters.

Parameter	Value
$s_d^{(5)}$	0.277
$s_d^{(7)}$	0.388
S_C	23 m^2
α	0.420

Using the approach with apparent levels of ingestions, the amplification factor β may change from thruster to thruster, pressure levels, and the method with which the $\Delta\dot{m}^{(app)}$ (e.g., from the discharge current variations) is calculated. In our case, with the same parameter β for all the three configurations, the error stayed within $\pm1\%$, as shown in Figure 14. However, it must be said that the β can be calibrated for each configuration to obtain a better fit.
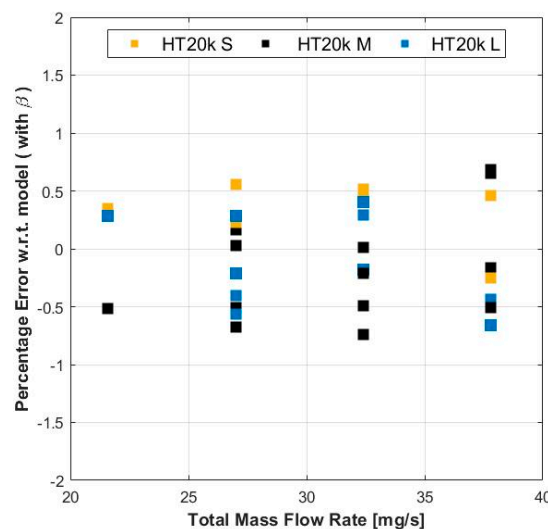

Figure 14. Percentage error regarding the model (with $\beta = 49.6$) for all 3 configurations; the $\Delta\dot{m}^{(app)}_{7-5}$ was calculated from thrust variations.

The β calibrated with the data of all the three configuration turned out to be 49.6. This means that, in order to explain the change in performance due to only ingested mass flow rate, the effective ingestion area of the channel would be almost fifty times larger than the actual annular surface πdb.

Since the value of β was much greater than 1, it was clear that the ingestion, ionization, and acceleration of background neutrals were not sufficient to justify the change of thruster performance. The apparent levels of ingestion used to explain the change in performace would thus be far from what would be the actual and real ingested mass flow rate. This implies that there are other phenomena that come into play when the physics of a vacuum chamber are coupled with the physics of the Hall thruster, leading to a change of the γ_I and γ_T with pressure.

Considering $\beta = 1$, and thus the actual anular exit surface, the ingested mass flow rates values with five and seven cold panels are plotted in Figure 15. Those values were within the error of the anode mass flow controller. Even if the ingested mass flow rates are small and can be neglected from Equation (22), their effect (as the effect of the low density particles coming in the upstream direction) cannot. As a consequence, Equation (22) becomes:

$$\begin{cases} \dfrac{I_d^{(5)}-I_d^{(7)}}{I_d^{(7)}} = \dfrac{\gamma_I^{(5)}-\gamma_I^{(7)}}{\gamma_I^{(7)}} = \dfrac{\gamma_I^{(5)}}{\gamma_I^{(7)}} - 1 \\[4mm] \dfrac{T^{(5)}-T^{(7)}}{T^{(7)}} = \dfrac{\gamma_T^{(5)}-\gamma_T^{(7)}}{\gamma_T^{(7)}} = \dfrac{\gamma_T^{(5)}}{\gamma_T^{(7)}} - 1 \end{cases}. \tag{25}$$
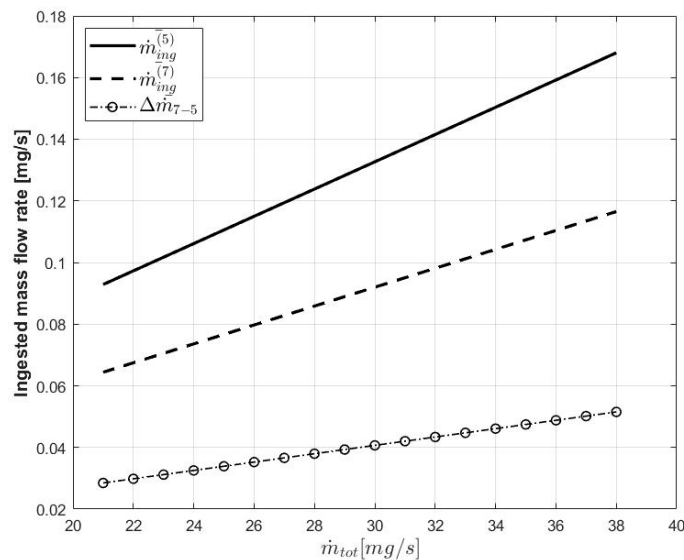

Figure 15. Ingested mass flow rates, computed by the background flow model for the HT20k M and considering $\beta = 1$.

For γ_I, we can say that:

$$\frac{\gamma_I^{(5)}}{\gamma_I^{(7)}} = \frac{\eta_m^{(5)} \sum (\xi_i^{(5)} Z_i)\, \eta_{current}^{(7)}}{\eta_m^{(7)} \sum (\xi_i^{(7)} Z_i)\, \eta_{current}^{(5)}} \tag{26}$$

Since the Faraday probe scans measured a negligible change in $\eta_{current}$, the performance variation could be linked to a change in the product $\eta_m \sum(\xi_i Z_i)$.

For the γ_T, we get:

$$\frac{\gamma_T^{(5)}}{\gamma_T^{(7)}} = \frac{\eta_m^{(5)} \psi_T^{(5)} \sqrt{\eta_v^{(5)}} \sum (\xi_i^{(5)} \sqrt{Z_i})}{\eta_m^{(7)} \psi_T^{(7)} \sqrt{\eta_v^{(7)}} \sum (\xi_i^{(7)} \sqrt{Z_i})} \tag{27}$$

Since we did not find a significant difference in the divergence, the factor ψ_T can be thought to be constant, and the change in the γ_T can be linked to the change in the product $\eta_m \sqrt{\eta_v} \sum \left(\xi_i \sqrt{Z_i} \right)$.

The variations of γ_I and γ_T could be related to the plasma response to the change of pressure. Recent studies have found that a shift of the ionization and acceleration region is a cause in this change of performance [25,30,32,57], in addition to cathode coupling [33,34,58]. Furthermore, the particle density of the neutral particles in the proximity of the channel can be comparable to the particle density of the incoming flow. This, in turn, can lead to a change in the electron mobility in the ionization, acceleration, and near plume regions [3,59]. The latter can also explain the change of the plasma oscillations characteristics of the thruster [60].

Future work will be dedicated to an in-depth study of the physics in the proximity of the channel exit to quantify these changes.

5. Conclusions

A 20 kW-class magnetically shielded Hall thruster was characterized in a SITAEL IV10 vacuum facility. The thruster can be assembled in three configurations with discharge channels of different widths (L > M > S) and a different set of magnetic screens and poles to have the same shielded topology.

The characterization was carried out at fixed anode mass flow rates and at fixed cathode-to-anode mass flow rate ratio (i.e., 8%). The same operative points were repeated with higher pumping speeds and lower pressure levels, and a reduction of the discharge current and thrust was noticed. After analyzing the pressure levels, an estimate of the effective pumping speed and sticking coefficient of the pumps was carried out. The Faraday scans and the discharge current oscillation amplitudes at the two pumping speed levels were also presented. The Faraday scans did not show a significant change in the plume divergence and current utilization efficiency when changing from five to seven panels for each operating point. The cathode to ground voltage values were also presented. Since the channel area of the HT20k DM2 is larger in respect to Hall thrusters of lower power levels, the impact of the ingested mass flow rate could be considerable, and an analysis of the collected data was carried out.

By analyzing the change in the discharge current and thrust, a preliminary estimate of the propellant ingested by the thruster was performed, assuming that the change in performance was only related to a variation of the processed mass flow. The computed apparent levels of ingestions were then compared to an existing state of the art 1D background flow model. The results showed that, in order to explain the change in performance with only a change in the propellant mass flow, the thruster would have to collect on an area that was significantly larger than the channel frontal area. The present results thus indicated that the mechanism of background neutral ingestion is not sufficient to justify the change of thruster performance and that, as previously found out with other Hall thrusters, different mechanisms should be considered. In particular, the increase of background neutral particles may have a significant impact on the plasma properties and electron cross-field mobility, inducing a shift of the thruster acceleration region.

Further work is needed to study and characterize the plasma discharge and the mechanisms that relate thruster performance and background pressure. In particular, there is a need to investigate the physics of the discharge and to obtain a better understanding of the neutral dynamics in the neighborhood of the thruster. From the point of view of technology development and qualification, the results of this wok highlight the need for testing at adequate pressure levels, in the order of 10^{-4} Pa.

Author Contributions: Conceptualization, A.P. (Antonio Piragino), T.A.; methodology, A.P. (Antonio Piragino); data curation, A.P. (Antonio Piragino), F.F., M.R., E.F., A.P. (Annalisa Piraino); writing—original draft preparation, A.P. (Antonio Piragino), F.F., M.R., E.F.; writing—review and editing, A.P. (Antonio Piragino), T.A.; supervision, T.A. All authors have read and agreed to the published version of the manuscript.

Appendix A

A summary of the results of the Faraday probe scans and CRP values is presented here.

Table A1. λ and $\eta_{current}$ for the various operative conditions for HT20k M.

Operative Point		5 Panels		7 Panels	
$\dot{m}_a$ [mg/s]	V_d [V]	$\lambda^{(5)}$ [rad]	$\eta_{current}^{(5)}$	$\lambda^{(7)}$ [rad]	$\eta_{current}^{(7)}$
25	250	0.54 ± 0.02	0.77 ± 0.02	0.53 ± 0.02	0.76 ± 0.02
30	250	0.54 ± 0.02	0.76 ± 0.02	0.53 ± 0.02	0.75 ± 0.02
35	250	0.56 ± 0.02	0.77 ± 0.02	0.56 ± 0.02	0.77 ± 0.02
20	300	0.51 ± 0.02	0.80 ± 0.02	0.50 ± 0.02	0.80 ± 0.02
25	300	0.51 ± 0.02	0.80 ± 0.02	0.50 ± 0.02	0.80 ± 0.02
30	300	0.51 ± 0.02	0.79 ± 0.02	0.51 ± 0.02	0.80 ± 0.02
35	300	0.54 ± 0.02	0.80 ± 0.02	0.54 ± 0.02	0.82 ± 0.02
25	400	0.46 ± 0.02	0.84 ± 0.02	0.44 ± 0.02	0.85 ± 0.02
30	400	0.49 ± 0.02	0.83 ± 0.02	0.49 ± 0.02	0.84 ± 0.02
35	400	0.50 ± 0.02	0.83 ± 0.02	0.49 ± 0.02	0.84 ± 0.02
25	500	0.49 ± 0.02	0.90 ± 0.02	0.48 ± 0.02	0.91 ± 0.02
30	500	0.51 ± 0.02	0.91 ± 0.02	0.50 ± 0.02	0.91 ± 0.02
35	500	0.53 ± 0.02	0.90 ± 0.02	0.53 ± 0.02	0.91 ± 0.02

Table A2. RMS/I_d for the various operative conditions of the HT20k M.

Operative Point		5 Panels	7 Panels
$\dot{m}_a$ [mg/s]	V_d [V]	RMS/I_d [%]	RMS/I_d [%]
25	250	4.4	2.8
30	250	3.7	2.3
35	250	4.1	1.9
20	300	6.1	1.9
25	300	5.1	2.3
30	300	4.7	2.2
35	300	4.1	1.9
25	400	21.9	15.3
30	400	20.5	7.6
35	400	13.8	4.4
25	500	23.1	19
30	500	19.2	16.3
35	500	23.6	14

Table A3. CRP (cathode reference potential) for the various operative conditions of the HT20k M.

Operative Point		5 Panels	7 Panels
$\dot{m}_a$ [mg/s]	V_d [V]	*CRP* [V]	*CRP* [V]
25	250	-8.6 ± 0.3	-9.6 ± 0.3
30	250	-7.5 ± 0.3	-9.3 ± 0.3
35	250	-7.0 ± 0.3	-9.0 ± 0.3
20	300	-9.6 ± 0.3	-10.3 ± 0.3
25	300	-8.1 ± 0.3	-8.3 ± 0.3
30	300	-6.7 ± 0.3	-8.2 ± 0.3
35	300	-6.5 ± 0.3	-8.0 ± 0.3
25	400	-11.7 ± 0.3	-12.8 ± 0.3
30	400	-9.1 ± 0.3	-10.7 ± 0.3
35	400	-8.9 ± 0.3	-9.1 ± 0.3
25	500	-16.1 ± 0.3	-14 ± 0.3
30	500	-13.8 ± 0.3	-12.8 ± 0.3
35	500	-11.8 ± 0.3	-12.5 ± 0.3

References

1. Levchenko, I.; Xu, S.; Mazouffre, S.; Lev, D.; Pedrini, D.; Goebel, D.; Garrigues, L.; Taccogna, F.; Bazaka, K. Perspectives, frontiers, and new horizons for plasma-based space electric propulsion. *Phys. Plasmas* **2020**, *27*, 020601. [CrossRef]
2. Mazouffre, S. Electric propulsion for satellites and spacecraft: Established technologies and novel approaches. *Plasma Sources Sci. Technol.* **2016**, *25*, 033002. [CrossRef]
3. Boeuf, J.-P. Tutorial: Physics and modeling of Hall thrusters. *J. Appl. Phys.* **2017**, *121*, 011101. [CrossRef]
4. Levchenko, I.; Xu, S.; Wu, Y.-L.; Bazaka, K. Hopes and concerns for astronomy of satellite constellations. *Nat. Astron.* **2020**, *4*, 1012–1014. [CrossRef]
5. Anonymous. Sustainable space mining. *Nat. Astron.* **2019**, *3*, 465. [CrossRef]
6. Kim, V.; Popov, G.; Arkhipov, B.; Murashko, V.; Gorshkov, O.; Koroteyev, A.; Garkusha, V.; Semenkin, A.; Tverdokhlebov, S. Electric Propulsion Activity in Russia. In Proceedings of the 27th International Electric Propulsion Conference (IEPC), Pasadena, CA, USA, 15–19 October 2001; IEPC-01-05.
7. Arkhipov, B.A.; Veoelovzorov, A.N.; Gavryushin, V.M.; Khartov, S.A.; Kim, V.; Kozlov, V.I.; Maslennikov, N.A.; Morozov, A.I.; Murashko, V.M.; Pokrovski, I.B. Development and Investigation of Characteristics of Increased Power SPT Models. In Proceedings of the International Electric Propulsion Conference, Seattle, WA, USA, 13–16 September 1993; IEPC-93-222.
8. Jankovsky, R.S.; McLean, C.; McVey, J. Preliminary Evaluation of a 10kW Hall Thruster. In Proceedings of the 37th Aerospace Sciences Meeting and Exhibit, Reno, NV, USA, 11–14 January 1999; AIAA-99-0456. [CrossRef]
9. Manzella, D.H.; Jankovsky, R.S.; Hofer, R. Laboratory Model 50 kW Hall Thruster. In Proceedings of the 38th AIAA/ASME/SAE/ASEE Joint Propulsion Conference & Exhibit, Indianapolis, IN, USA, 7–10 July 2002; AIAA 2002-3676. [CrossRef]
10. Peterson, P.Y.; Jacobson, D.T.; Manzella, D.H.; John, J.W. The Performance and Wear Characterization of a High-Power High-Isp NASA Hall Thruster. In Proceedings of the 41st AIAA/ASME/SAE/ASEE Joint Propulsion Conference & Exhibit, Tucson, AZ, USA, 10–13 July 2005; AIAA 2005-4243. [CrossRef]
11. Kamhawi, H.; Haag, T.W.; Jacobson, D.T.; Manzella, D.H. Performance Evaluation of the NASA-300M 20 kW Hall Effect Thruster. In Proceedings of the 47th AIAA/ASME/SAE/ASEE Joint Propulsion Conference & Exhibit, San Diego, CA, USA, 31 July–3 August 2011; AIAA 2011-5521. [CrossRef]
12. Kamhawi, H.; Huang, W.; Haag, T.; Shastry, R.; Soulas, G.; Smith, T.; Mikellides, I.G.; Hofer, R.R. Performance and Thermal Characterization of the NASA300MS 20 kW Hall Effect Thruster. In Proceedings of the IEPC, Washington, DC, USA, 6–10 October 2013; IEPC-2013-444.
13. Szabo, J.; Pote, B.; Hruby, V.; Byrne, L.; Tedrake, R.; Kolencik, G. A Commercial One Newton Hall Effect Thruster for High Power in Space Missions. In Proceedings of the 47th AIAA/ASME/SAE/ASEE Joint Propulsion Conference & Exhibit, San Diego, CA, USA, 31 July–3 August 2011; AIAA 2011-6152. [CrossRef]
14. Pyatykh, I.N.; Bernikova, M.Y.; Gopanchuk, V.V.; Gnizdor, R.Y.; Zhasan, V.S.; Katashova, M.I.; Savchenko, K.A. Development of stationary plasma thruster SPT-230 with discharge power of 10–15 Kw. In Proceedings of the 35th International Electric Propulsion Conference (IEPC), Atlanta, GA, USA, 8–12 October 2017; IEPC-2017-548.
15. Zubair, J. Development of a 12.5kW Hall Thruster for Advanced Electric Propulsion System. In Proceedings of the AIAA Propulsion and Energy 2020 Forum, New Orleans, LA, USA, 24–28 August 2020; AIAA 2020-3628. [CrossRef]
16. Available online: https://www1.grc.nasa.gov/facilities/eppl/#facility-overview (accessed on 14 January 2021).

17. Peterson, P.Y.; Kamhawi, H.; Huang, W.; Yim, J.; Haag, T.; Mackey, J.; McVetta, M.; Sorrelle, L.; Tomsik, T.; Gillagan, R.; et al. Reconfiguration of NASA GRC's Vacuum Facility 6 for Testing of Advanced Electric Propulsion System (AEPS) Hardware. In Proceedings of the 35th International Electric Propulsion Conference Georgia Institute of Technology, Atlanta, GA, USA, 8–12 October 2016; IEPC-2017-028.

18. Viges, E.A.; Jorns, B.A.; Gallimore, A.D.; Sheehan, J.P. University of Michigan's Upgraded Large Vacuum Test Facility. In Proceedings of the 36th International Electric Propulsion Conference, Vienna, Austria, 15–20 September 2019; IEPC-2019-653.

19. Available online: https://www.sitael.com/space/advanced-propulsion/electric-propulsion/tools-services/ (accessed on 14 January 2021).

20. Randolph, T.; Kim, V.; Kaufman, H.; Kozubky, K.; Zhurin, V.; Day, M. Facility Effects on Stationary Plasma Thruster Testing. In Proceedings of the 23rd International Electric Propulsion Conference, Seattle, WA, USA, 13–16 September 1993; IEPC-93-93.

21. Reid, B.M. The Influence of Neutral Flow Rate in the Operation of Hall Thrusters. Ph.D. Thesis, Aerospace Egineerng Department, University of Michigan, Ann Arbor, MI, USA, 2009; pp. 306–319.

22. Walker, M.L.R.; Gallimore, A.D. Performance Characteristics of a Cluster of 5-kW Laboratory Hall Thrusters. *J. Propuls. Power* **2007**, *23*, 35–43. [CrossRef]

23. Hofer, R.R.; Anderson, J.R. Finite Pressure Effects in Magnetically Shielded Hall Thrusters. In Proceedings of the 50th AIAA/ASME/SAE/ASEE Joint Propulsion Conference, Cleveland, OH, USA, 28–30 July 2014; AIAA 2014-3709. [CrossRef]

24. Diamant, K.D.; Liang, R.; Corey, R.L. The Effect of Background Pressure on SPT-100 Hall Thruster Performance. In Proceedings of the 50th AIAA/ASME/SAE/ASEE Joint Propulsion Conference, Cleveland, OH, USA, 28–30 July 2014; AIAA 2014-3710. [CrossRef]

25. Huang, W.; Kamhawi, H.; Lobbia, R.B.; Brown, D.L. Effect of Background Pressure on the Plasma Oscillation Characteristics of the HiVHAc Hall Thruster. In Proceedings of the 50th AIAA/ASME/SAE/ASEE Joint Propulsion Conference, Cleveland, OH, USA, 28–30 July 2014; AIAA 2014-3708. [CrossRef]

26. Snyder, J.S.; Lenguito, G.; Frieman, J.D.; Haag, T.W.; Mackey, J.A. Effects of Background Pressure on SPT-140 Hall Thruster Performance. *J. Propuls. Power* **2020**, *36*, 668–676. [CrossRef]

27. Cusson, S.E. Impact of the Neutral Density on the Operation of High-Power Magnetically Shielded Hall Thrusters. Ph.D. Thesis, University of Michigan, Ann Arbor, MI, USA, 2019.

28. Reid, B.M. Empirically-Derived Corrections for Facility Effects in Performance and Plume Measurements of Hall Thrusters. In Proceedings of the 34th International Electric Propulsion Conference, Seattle, WA, USA, 13–16 September 1993; IEPC 2015-362.

29. Walker, M.L.R.; Gallimore, A.D. Neutral density map of Hall thruster plume expansion in a vacuum chamber. *Rev. Sci. Instrum.* **2005**, *76*, 053509. [CrossRef]

30. Nakles, M.R.; Hargus, W.A. Background Pressure Effects on Ion Velocity Distribution Within a Medium-Power Hall Thruster. *J. Propuls. Power* **2011**, *27*, 737–743. [CrossRef]

31. Cusson, S.E.; Jorns, B.A.; Gallimore, A.D. Non-invasive in situ measurement of the near-wall ion kinetic energy in a magnetically shielded Hall thruster. *Plasma Sources Sci. Technol.* **2019**, *28*, 105012. [CrossRef]

32. Cusson, S.E.; Dale, E.T.; Jorns, B.A.; Gallimore, A.D. Acceleration region dynamics in a magnetically shielded Hall thruster. *Phys. Plasmas* **2019**, *26*, 023506. [CrossRef]

33. Spektor, R.; Tighe, W.G.; Stoltz, P.H.; Beckwith, K.R.C. Facility Effects on Hall Thruster Performance through Cathode Coupling. In Proceedings of the Joint Conference of 30th International Symposium on Space Technology and Science, 34th International Electric Propulsion Conference and 6th Nano-satellite Symposium, Hyogo-Kobe, Japan, 4–10 July 2015; IEPC-2015-309/ISTS-2015-b-309.

34. Jorns, B.A.; Byrne, M. Model for the dependence of cathode voltage in a Hall thruster on facility pressure. *Plasma Sources Sci. Technol.* **2020**, *30*, 015012. [CrossRef]

35. Dale, E.; Jorns, B.; Gallimore, A. Future Directions for Electric Propulsion Research. *Aerospace* **2020**, *7*, 120. [CrossRef]

36. Huang, W.; Kamhawi, H.; Haag, T. Facility Effect Characterization of NASA's HERMeS Hall Thruster. In Proceedings of the 52nd AIAA/SAE/ASEE Joint Propulsion Conference, Salt Lake City, UT, USA, 25–27 July 2016; AIAA 2016-4828. [CrossRef]

37. Paissoni, C.; Viola, N.; Mammarella, M.; Andreussi, T.; Rossodivita, A.; Saccoccia, G. Deep space transportation enhanced by 20 kW-Class Hall Thrusters. *Acta Astronaut.* **2020**, *171*, 83–96. [CrossRef]

38. Piragino, A.; Ferrato, E.; Faraji, F.; Reza, M.; Andreussi, T.; Rossodivita, A.; Andrenucci, M. Experimental Characterization of a 5kW Magnetically Shielded Hall Thruster. In Proceedings of the Space Propulsion Conference 2018, Seville, Spain, 16–18 May 2018; SP2018_427.

39. Saravia, M.M.; Giacobbe, A.; Andreussi, T. Bayesian analysis of triple Langmuir probe measurements for the characterization of Hall thruster plasmas. *Rev. Sci. Instrum.* **2019**, *90*, 023502. [CrossRef]

40. Giannetti, V.; Ferrato, E.; Piragino, A.; Reza, M.; Faraji, F.; Andrenucci, M.; Andreussi, T. HT5k Thruster Unit Development History, Status and Way Forward. In Proceedings of the 36th International Electric Propulsion Conference, Vienna, Austria, 15–20 September 2019; IEPC-2019-878.

41. Andreussi, T.; Giannetti, V.; Leporini, A.; Saravia, M.M.; Andrenucci, M. Influence of the magnetic field configuration on the plasma flow in Hall thrusters. *Plasma Phys. Control. Fusion* **2017**, *60*, 014015. [CrossRef]

42. Piragino, A.; Leporini, A.; Giannetti, V.; Pedrini, D.; Rossodivita, A.; Andreussi, T.; Andrenucci, M. Characterization of a 20 kW-class Hall Effect Thruster. In Proceedings of the 35th International Electric Propulsion Conference, Atlanta, GA, USA, 8–12 October 2017; IEPC-2017-381.
43. Pedrini, D.; Misuri, T.; Paganucci, F.; Andrenucci, M. Development of Hollow Cathodes for Space Electric Propulsion at Sitael. *Aerospace* **2017**, *4*, 26. [CrossRef]
44. Saverdi, M.; Signori, M.; Milaneschi, L.; Cesari, U.; Biagioni, L. The IV10 Space Simulator for High Power Electric Propulsion Testing: Performance Improvements and Operation Status. In Proceedings of the 30th International Electric Propulsion Conference, Florence, Italy, 17–20 September 2007; IEPC-2007-321.
45. Piragino, A.; Giannetti, V.; Reza, M.; Faraji, F.; Ferrato, E.; Kitaeva, A.; Pedrini, D.; Andreussi, T.; Paganucci, F.; Andrenucci, M. Development Status of SITAEL's 20 kW Class Hall Thruser. In Proceedings of the AIAA Propulsion and Energy 2019 Forum, Indianapolis, IN, USA, 19–22 August 2019; AIAA-2019-3812. [CrossRef]
46. Walker, M.L.R. *Effects of Facility Backpressure on the Performance and Plume of a Hall Thruster*; The University of Michigan: Ann Arbor, MI, USA, 2005; pp. 56–57.
47. Brown, D.L.; Walker, M.L.R.; Szabo, J.; Huang, W.; Foster, J.E. Recommended Practice for Use of Faraday Probes in Electric Propulsion Testing. *J. Propuls. Power* **2017**, *33*, 582–613. [CrossRef]
48. Frieman, J.D.; Liu, T.M.; Walker, M.L.R. Background Flow Model of Hall Thruster Neutral Ingestion. *J. Propuls. Power* **2017**, *33*, 1–15. [CrossRef]
49. Frieman, J.D. Characterization of Background Neutral Flow in Vacuum Test Facilities and Impact on Hall Effect Thruster Operation. Ph.D. Thesis, Georgia Institute of Technology, Atlanta, GA, USA, August 2017.
50. Cai, C.; Boyd, I.; Sun, Q. Rarefied Background Flow in a Vacuum Chamber Equipped with One-Sided Pumps. *J. Thermophys. Heat Transf.* **2006**, *20*, 524–535. [CrossRef]
51. Hofer, R.R. Development and Characterization of High-Efficiency, High-Specific Impulse Xenon Hall Thrusters. Ph.D. Thesis, University of Michigan, Ann Arbor, MI, USA, 2004.
52. Piragino, A.; Ferrato, E.; Faraji, F.; Reza, M.; Giannetti, V.; Kitaeva, A.; Pedrini, D.; Andrenucci, M.; Andreussi, T. SITAEL's Magnetically Shielded 20 kW Hall Thruster Tests. In Proceedings of the 36th International Electric Propulsion Conference, Vienna, Austria, 15–20 September 2019; IEPC-2019-879.
53. Andreussi, T.; Piragino, A.; Reza, M.; Giannetti, V.; Farajii, F.; Ferrato, E.; Pedrini, D.; Kitaeva, A.; Rossodivita, A.; Andrenucci, M.; et al. Development status and way forward of SITAEL's 20kW class Hall Thruster, the HT20k. In Proceedings of the 36th International Electric Propulsion Conference, Vienna, Austria, 15–20 September 2019; IEPC-2019-825.
54. Cai, C. Theoretical and Numerical Studies of Plume Flows in a Vacuum Chamber. Ph.D. Thesis, University of Michigan, Ann Arbor, MI, USA, 2005.
55. Dankanich, J.W.; Walker, M.; Swiatek, M.W.; Yim, J.T. Recommended Practice for Pressure Measurement and Calculation of Effective Pumping Speed in Electric Propulsion Testing. *J. Propuls. Power* **2017**, *33*, 668–680. [CrossRef]
56. Andrenucci, M. Arcjet Modeling and Engine Health Monitoring. In Proceedings of the 30th Joint Propulsion Conference and Exhibit, Indianapolis, IN, USA, 27–29 June 1994; AIAA-94-3007. [CrossRef]
57. Peng, E.; Yu, D.; Jiang, B. Experimental Investigation of Backpressure Effects on the Ionization and Acceleration Processes in a Hall Thruster. In Proceedings of the 31th International Electric Propulsion Conference, Ann Arbor, MI, USA, 20–24 September 2009; IEPC 2009-119.
58. Cusson, S.E.; Jorns, B.A.; Gallimore, A.D. Simple Model for Cathode Coupling Voltage versus Background Pressure in a Hall Thruster. In Proceedings of the 53rd AIAA/SAE/ASEE Joint Propulsion Conference, Atlanta, GA, USA, 10–12 July 2017; AIAA 2017-4889. [CrossRef]
59. Jorns, B.A.; Hofer, R.R.; Mikellides, I.G. Power Dependence of the Electron mobility profile in a Hall Thruster. In Proceedings of the 50th AIAA/ASME/SAE/ASEE Joint Propulsion Conference, Cleveland, OH, USA, 28–30 July 2014; AIAA 2014-3620. [CrossRef]
60. Choueiri, E.Y. Plasma oscillations in Hall thrusters. *Phys. Plasmas* **2001**, *8*, 1411. [CrossRef]